CrystEngComm

PAPER

View Article Online
View Journal | View Issue

Cite this: *CrystEngComm*, 2016, **18**, 6184

Enormous lattice distortion through an isomorphous phase transition in an organic–inorganic hybrid based on haloantimonate(III)†

Martyna Wojciechowska,[a] Przemysław Szklarz,[a] Agata Białońska,[a] Jan Baran,[b] Rafał Janicki,[a] Wojciech Medycki,[c] Piotr Durlak,[a] Anna Piecha-Bisiorek*[a] and Ryszard Jakubas[a]

Bis(diisobutylammonium) octabromodiantimonate(III), $[(i\text{-}C_4H_9)_2NH_2]_2Sb_2Br_8$, has been synthesized. The differential scanning calorimetric measurements indicate a reversible, first-order phase transition at 222/229 K (cooling/heating). The single crystal X-ray diffraction studies reveal that the phase transition is isomorphous and is accompanied by a huge distortion of the crystal lattice. By comparison of the crystal structures of $[(i\text{-}C_4H_9)_2NH_2]_2Sb_2Br_8$ and $[(i\text{-}C_4H_9)_2NH_2]_2Sb_2Cl_8$, an analogous mechanism of the phase transition of the former is proposed. The change of the electronic structure of the complex during the phase transition was analyzed by UV-vis spectroscopy. A low-frequency dielectric relaxation process appears over phase I (below the room temperature) and corresponds to the dynamics of dipolar diisobutylammonium cations. The detailed analysis of the molecular motions of the organic cations studied by means of proton magnetic resonance (^{1}H NMR) in a wide temperature range indicates a leading role of the methyl groups in the relaxation mechanism. A variable-temperature investigation of the infrared spectra of $[(i\text{-}C_4H_9)_2NH_2]_2Sb_2Br_8$ confirms, in turn, the influence of the diisobutylammonium cation dynamics on the molecular mechanism of the structural transformation at 229 K.

Received 29th April 2016,
Accepted 27th June 2016

DOI: 10.1039/c6ce01008c

www.rsc.org/crystengcomm

Introduction

The compounds of haloantimonates(III) and halobismuthates(III) with amines have been known for over a century. Current interest in these compounds stems from their possible applications as nonlinear optical (NLO) and nonlinear dielectric (polar) materials.[1–12] During the past 25 years, in the family of crystals described by the formula $R_aM_bX_{(3b+a)}$ (X = Cl, Br, I; M = Sb(III), Bi(III) and R is an organic cation), a dozen of novel ferroelectrics have been obtained. In spite of the fact that haloantimonates(III) and halobismuthates(III) are characterized by a rich diversity of the anionic networks in the crystal lattices, the ferroelectric properties are limited only to several chemical stoichiometries namely: $R_5M_2X_{11}$,[13–17] $R_3M_2X_9$,[18–21] R_2MX_5 (ref. 22 and 23) and RMX_4,[24,25] where the cations are usually small alkylammonium ones or five and six-membered heteroaromatic rings. In general, most of the paraelectric–ferroelectric phase transitions (PTs) are characterized by an 'order–disorder' mechanism connected with the dynamics of the organic counterions.

In our search for new acentric and switchable dielectric PT materials, we have extended our studies on derivatives containing bulky secondary aliphatic amines. It should be emphasized that simple (1 : 1) ionic compounds built from expanded secondary aliphatic amines, for example diisopropylammonium chloride[26] and diisopropylammonium bromide,[27,28] are very promising room temperature ferroelectric materials with spontaneous polarization comparable with those of well known perovskite-like ferroelectrics ($BaTiO_3$). Diisobutylamine molecules are characterized by a significant dipole moment, which makes them good candidates as components in inorganic–organic hybrid compounds. A change in the dynamics/reorientation of such dipolar units in the crystal lattice may lead to interesting dielectric properties (a tunable and switchable dielectric constant) and PTs.[29]

Here we present two novel organic–inorganic hybrid materials, diisobutylammonium analogs based on haloantimonates(III); $[(i\text{-}C_4H_9)_2NH_2]_2Sb_2Cl_8$ and $[(i\text{-}C_4H_9)_2NH_2]_2Sb_2Br_8$. As it turned out only the latter compound was found to undergo isomorphous structural PT of the first-order at 222 K (cooling). The

---

[a] Faculty of Chemistry, University of Wrocław, Joliot-Curie 14, 50-383 Wrocław, Poland. E-mail: anna.piecha@chem.uni.wroc.pl

[b] Institute of Low Temperature and Structure Research, Polish Academy of Science, Okólna 2, PO Box 937, 50-950 Wrocław 2, Poland

[c] Institute of Molecular Physics, Polish Academy of Science, M. Smoluchowskiego 17, 60-179 Poznań, Poland

† Electronic supplementary information (ESI) available: Crystal structure, thermal, optical and dielectric properties as well as proton magnetic resonance (^{1}H NMR) and IR studies. CCDC 1475468–1475471. For ESI and crystallographic data in CIF or other electronic format see DOI: 10.1039/c6ce01008c

proposed mechanism of the PT was based on the thermal, vibrational (IR) and dielectric studies, while the molecular motions of diisobutylammonium cations in $[(i\text{-}C_4H_9)_2NH_2]_2Sb_2Br_8$ were studied by means of proton magnetic resonance (^1H NMR) spectroscopy. The comparison of the crystal structures between the bromide (two phases) and the chloride compounds allowed us to explain/propose the origin of the PT in $[(i\text{-}C_4H_9)_2NH_2]_2Sb_2Br_8$.

Results and discussion

DSC measurements, presented in Fig. 1(a), indicate the presence of a perfectly reversible first-order structural PT which is characterized by a strong heat anomaly at about 222/229 K (cooling–heating) and thermal hysteresis (ΔT = 7 K). The entropy change (ΔS_{tr}) was estimated to be *ca.* 26 J mol^{-1} K^{-1}. It should be also added that a study of the phase situation based on dilatometric measurement (see Fig. S1 – ESI†) confirms the sequence and the nature of the low-temperature PT. The observation of the single crystal sample under a polarized microscope in the *ac* plane disclosed a characteristic phase front which shifts along the *a*-axis as it can be seen in Fig. S2.† It confirms the first-order character of the PT at 222 K. The optical observations disclose also an additional feature of the title compound which is related to the mechanical instability around T_c. Attached films (F1) show that the discontinuous PT, which is related to the huge distortion of the inorganic substructure (see Table 1), affects the characteristic bending of the crystal sample. No reversible PT was detected in $[(i\text{-}C_4H_9)_2NH_2]_2Sb_2Cl_8$ below room temperature (RT).

Above RT, the compound shows complex thermal properties because the visible heat anomalies are only partially reversible and connected with a simultaneously weak decomposition of the sample (see Fig. S3†). Fig. 1(b) shows the TGA–DTA scan of the $[(i\text{-}C_4H_9)_2NH_2]_2Sb_2Br_8$ crystal between 300 and 700 K. The first two endothermic peaks at *ca.* 370 and 387 K correspond to the irreversible PTs detected by DSC (see also Fig. S3†). The next heat anomaly at 408 K is due to the melting of the sample and onset of the decomposition of the compound.

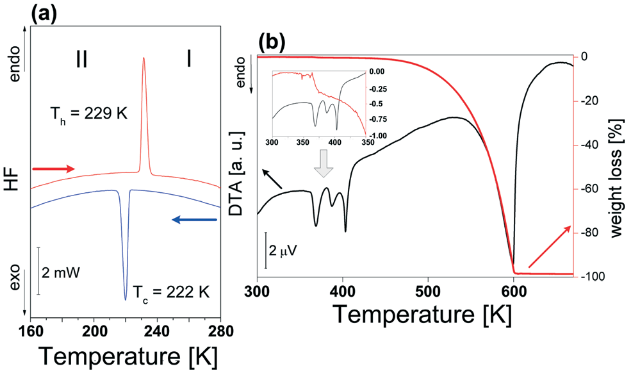

Fig. 1 (a) DSC traces upon cooling and heating (5 K min^{-1}) for $[(i\text{-}C_4H_9)_2NH_2]_2Sb_2Br_8$ (*m* = 9.822 mg); (b) simultaneous thermogravimetric and differential thermal analyses scan (ramp rate: 2 K min^{-1}).

Table 1 Selected Sb–Br bonds lengths (Å) and Sb–Br–Sb angles (°) for $[(i\text{-}C_4H_9)_2NH_2]_2Sb_2Br_8$

	Phase I (250 K)$_{exp.}$	Phase II (100 K)$_{calc.}$	Phase II (100 K)$_{exp.}$
Sb–Br(1)	2.5253(13)	2.6689	2.5261(9)
Sb–Br(2)	3.1196(14)	3.2718	3.0280(6)
Sb–Br(2)^i	3.174(2)	3.2864	3.3163(8)
Sb–Br(3)	2.5656(14)	2.5934	2.6170(5)
Sb–Br(4)	2.5476(18)	2.5659	2.5393(7)
Sb–Br(1)^{ii}	3.4918(16)	3.7214	3.6698(12)
Br(1)–Sb–Br(3)	93.33(4)	91.85	92.254(16)
Br(1)–Sb–Br(4)	95.55(7)	100.87	95.02(2)
Br(3)–Sb–Br(4)	93.48(4)	93.19	91.057(12)
Br(1)–Sb–Br(2)	86.80(3)	79.86	86.831(14)
Br(3)–Sb–Br(2)	176.66(4)	165.36	178.305(13)
Br(4)–Sb–Br(2)	89.83(3)	90.21	87.603(11)

Symmetry codes: ^{i} 1 − *x*, 1 − *y*, −*z*; ^{ii} 1 + *x*, *y*, *z*; exp. – X-ray diffraction; calc. – calculations.

Single-crystal X-ray diffraction and theoretical structure analysis

The single crystal X-ray diffraction experiment revealed that both phases of $[(i\text{-}C_4H_9)_2NH_2]_2Sb_2Br_8$ adopt the monoclinic $P2_1/c$ space group (no. 14). The independent portion of the unit cell at 250 K, together with the atom numbering scheme, is presented in Fig. 2(a). It consists of one diisobutylammonium cation and half of the $[Sb_2Br_8^{2-}]$ anion. In both phases all atoms occupy the general positions; however, the centre of gravity of the $[Sb_2Br_8^{2-}]$ anions is placed at the symmetry centre.

The centrosymmetric $[Sb_2Br_8^{2-}]$ ions consist of two distorted square pyramids sharing a basal edge (Fig. 2(a)). At 250 K, the diisobutylammonium cations reveal disorder, in which each isobutyl group is distributed between two sites (Fig. 2(a) and 3(b)). At 100 K (phase II), the disorder disappears and diisobutylammonium cations are fully ordered (Fig. 2(b) and 3(c)).

The components of the anionic network ($[Sb_2Br_8^{2-}]$ moieties) are stacked along the [100] direction (*a*-axis). The shortest Sb⋯Br distance between neighboring $[Sb_2Br_8^{2-}]$ units along the [100] direction, which is equal to 3.67 Å, suggests a possible halogen–metal interaction and leads to formation of anionic supramolecular ribbons (see Fig. 3(a), 4 and Table 1).

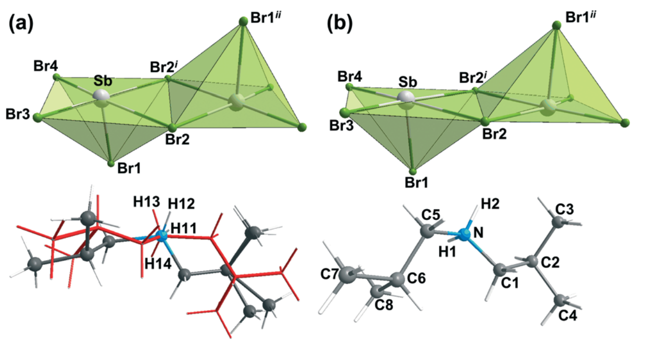

Fig. 2 The atom numbering scheme of $[(i\text{-}C_4H_9)_2NH_2]_2Sb_2Br_8$ at (a) 250 K and (b) 100 K (symmetry codes: ^{i} 1 − *x*, 1 − *y*, −*z*; ^{ii} 1 + *x*, *y*, *z*).

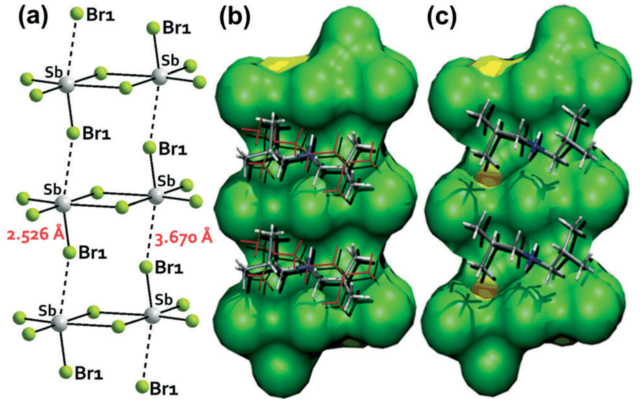

Fig. 3 (a) The supramolecular ribbon of the [$Sb_2Br_8{}^{2-}$] anionic moieties extended along the *a*-axis (phase II). The disordered (b) and ordered (c) diisobutylammonium cations in the grooves of the ribbon surface in the corresponding phases.

The diisobutylammonium cations are located in grooves of the supramolecular anionic ribbons, formed between neighboring [$Sb_2Br_8{}^{2-}$] units. The diisobutylammonium cations interact *via* N–H···Br hydrogen bonds with neighboring [$Sb_2Br_8{}^{2-}$] units additionally stabilizing the anionic supramolecular structure (Table 2). The relatively high thermal vibration factors of the terminal Br atoms in the high temperature phase indicate significant librational motions of the whole [$Sb_2Br_8{}^{2-}$] anions with respect to their symmetry centre. In the low-temperature phase II, the [$Sb_2Br_8{}^{2-}$] anions reduce significantly their librational motion. The PT is not accompanied by a change in the space group, thus this transition is classified as an isomorphous one.

The PT is accompanied by a huge distortion of the crystal lattice. After the transition, the dimensions of *a* and *c* of the unit cell increase by about 0.09 and 0.45 Å, respectively, whereas the dimension of *b* is significantly reduced by about 1.91 Å (above 9%). Also the *β* angle changes during the PT (decreases about 2.93°). The huge distortion of the crystal lattice during the PT does not lead to the breaking of the symmetry (see Table S1 – ESI†). Such an effect, rarely encountered, is a result of the fact that all the atoms of the ions are placed in general positions and anions are additionally situated at the symmetry centre. In consequence, even the huge distortion of the crystal lattice due to the PT retains the same symmetry (space group) of the phases II and I.

Table 2 Hydrogen bonds for $[(i\text{-}C_4H_9)_2NH_2]_2Sb_2Br_8$ [Å and °] (phase I/phase II)

D–H···A	*d*(D–H)	*d*(H···A)	*d*(D···A)	∠(DHA)
N–H(2)···Br(2)	0.99/0.91	2.54/2.60	3.386(7)/3.398(3)	143/147
calculated	—/1.02	—/2.69	—/3.621	—/150
N–H(1)···Br(2)^{i}	0.89/0.91	2.62/2.70	3.355(7)/3.540(3)	140/154
calculated	—/1.01	—/2.72	—/3.684	—/152

Symmetry code: ^{i} *x* − 1, *y*, *z*.

For better understanding of the mechanism of the PT and especially of the huge distortion of the crystal lattice observed for $[(i\text{-}C_4H_9)_2NH_2]_2Sb_2Br_8$ during the PT, we additionally synthesized and structurally characterized the $[(i\text{-}C_4H_9)_2NH_2]_2Sb_2Cl_8$ analog. The crystal structure of $[(i\text{-}C_4H_9)_2NH_2]_2Sb_2Cl_8$ is quite similar to $[(i\text{-}C_4H_9)_2NH_2]_2Sb_2Br_8$. However, the diisobutylammonium cations in $[(i\text{-}C_4H_9)_2NH_2]_2Sb_2Cl_8$ are ordered in the temperature range 100–250 K and the geometry as well as the mutual orientation of the [$Sb_2Cl_8{}^{2-}$] units remains without more significant changes (ESI†). The $[(i\text{-}C_4H_9)_2NH_2]_2Sb_2Cl_8$ does not reveal any PT in the temperature range of 100–250 K. The average Sb–Br distance in $[(i\text{-}C_4H_9)_2NH_2]_2Sb_2Br_8$ is about 0.13 Å greater than the average Sb–Cl distance in $[(i\text{-}C_4H_9)_2NH_2]_2Sb_2Cl_8$. This causes a weak fitting of the diisobutylammonium cations to the grooves of the anionic ribbons and leads to the disorder of the cations in $[(i\text{-}C_4H_9)_2NH_2]_2Sb_2Br_8$ at 250 K. However, at 100 K, some Sb–Br distances of [$Sb_2Br_8{}^{2-}$] units are even greater (even about 0.14 Å) than at 250 K, and diisobutylammonium cations are ordered. Simultaneously, after the PT in the cooling mode, the Br–Sb–Br angles of [$SbBr_4{}^{-}$] reveal a noticeable tendency to be closer to 90 or 180°, which is not observed in the $[(i\text{-}C_4H_9)_2NH_2]_2Sb_2Cl_8$ analog. Taking into account the changes of the Br–Sb–Br angles, the PT in the cooling mode

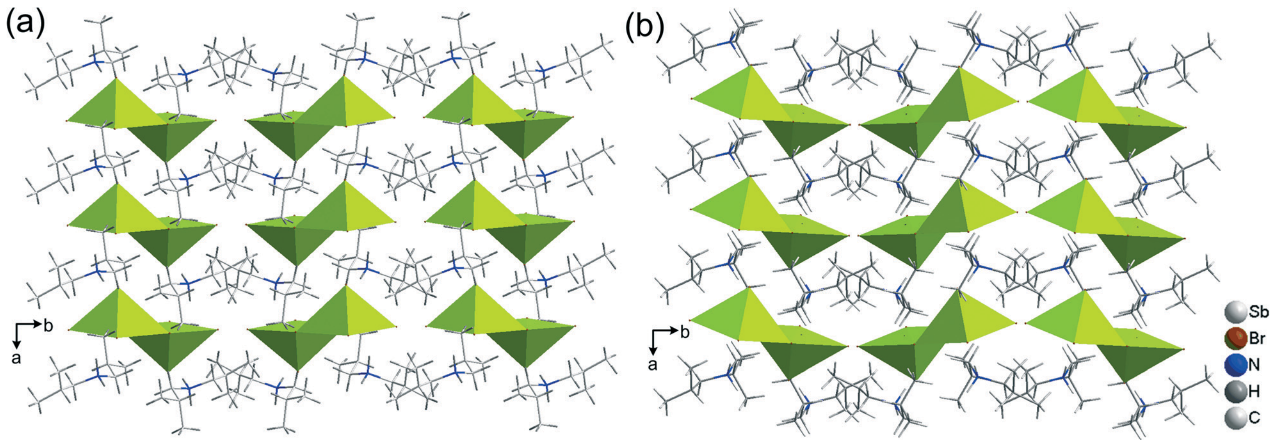

Fig. 4 Comparison of ion arrangement in phase I (left (a)) and phase II (right (b)).

is related to a smoothing of the anion distortion. The bridging Br2–Sb–Br2(1 − *x*, 1 − *y*, −*z*) angle does not follow this trend and the PT in the cooling mode leads to further deepening of the distortion of the Br2–Sb–Br2(1 − *x*, 1 − *y*, −*z*) angle. The PT in the cooling mode leads to differentiation of the Sb–Br bonds. The greatest changes of the Sb–Br distances are observed for the bridging Sb–Br2 and Sb–Br2(1 − *x*, 1 − *y*, −*z*) bonds. One is shortened about 0.09 Å and the other is elongated about 0.14 Å. Moreover, the [$Sb_2Br_8^{2-}$] units of the supramolecular ribbons are shifted with respect to each other. These changes make the grooves shallow, lead to better fitting of the cation and allow neighboring anionic ribbons to be closer to each other along the [011] and [0−11] directions. The PT is also accompanied by rotation of the [$Sb_2Br_8^{2-}$] units with respect to each other. At 250 K, the angle between basal planes of the [$Sb_2Br_8^{2-}$] units of neighboring ribbons is equal to 5.79° (Fig. 4(a)). At 100 K, the angle is equal to 25.47° (Fig. 4(b)). The reorientation of the [$Sb_2Br_8^{2-}$] units related to the change of the angle leads to additional shortening of the lattice constant *b*.

Full geometry and cell parameter optimisation for the solid state has been carried out to obtain the minimum structure of the [$(i\text{-}C_4H_9)_2NH_2]_2Sb_2Br_8$ crystal. The computational details are contained in the General section of this manuscript. The selected calculated results presented in Tables 1 and 2 show a good agreement with the X-ray diffraction data. Referring to Tables 1 and 2, it may be noticed that structural differences in the calculated and experimental parameters are small and do not exceed *ca.* 5%. The largest errors (*ca.* 6.4–8.0%) have been found for the calculated structural angles.

Moreover, the optimized parameters of the unit cell (a = 6.1949 Å, b = 17.0841 Å, c = 14.2261 Å, β = 95.77°) are in reasonable agreement with the experimental values (a = 6.046 Å, b = 18.1863 Å, c = 14.839 Å, β = 96.322°). For full comparison please see also Table S1.† This confirms the need to use dispersion corrections to the full energy for calculations on the DFT method level. The optimised structure of the investigated crystal was applied to calculate the frequencies in the IR and Raman spectra in the harmonic approximation. The calculation of the frequencies allows one to verify that the optimised structure is in the global minimum on the potential energy surface (PES).

UV-vis electronic spectroscopy

The structural changes of the [$Sb_2Br_8^{2-}$] complex modify the electronic structure of the complex. This should be reflected in the UV-vis electronic spectra. The spectra of the powdered compound under study are shown in Fig. 5. The RT spectrum of the isostructural [$(i\text{-}C_4H_9)_2NH_2]_2Sb_2Cl_8$ compound is also included in this figure for the purpose of comparison.

The spectra of the Sb^{3+} ion may be generally analyzed in terms of either the s → p transitions in the free Sb^{3+} ([Kr]$4d^{10}s^2$) ion[30] or the transitions between molecular orbitals of the [$Sb_2Br_8^{2-}$] complex.[31] The excited 5s5p configuration generates ^3P and ^1P levels which then branch into levels

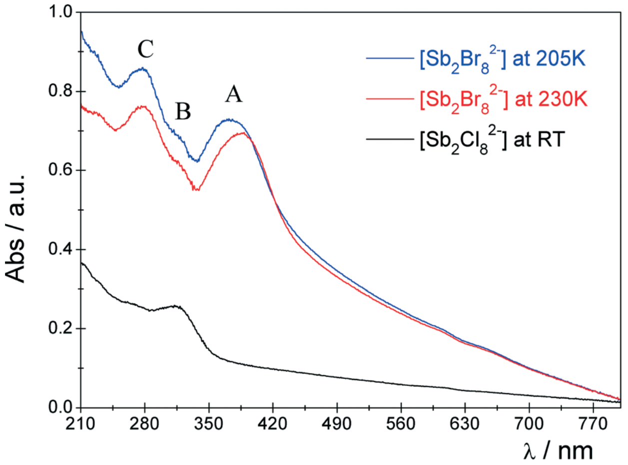

Fig. 5 UV-vis absorption spectrum of [$Sb_2Br_8^{2-}$] and [$Sb_2Cl_8^{2-}$] complexes.

in sequence of increasing energy ($^3P_0$, $^3P_1$, $^3P_2$, $^1P_1$) due to the spin–orbit coupling (Fig. 6(a)).[30]

For the case of the [$Sb_2Br_8^{2-}$] complex, which possesses C_s symmetry, all these transitions are symmetry allowed; however, due to the selection rules $\Delta S = 0$ and $\Delta J \neq 0$ and 2, the $^1S_0 \leftrightarrow {}^3P_0$ and $^1S_0 \leftrightarrow {}^3P_2$ transitions are forbidden.

Three well separated broad bands attributed to the $^1S_0 \rightarrow {}^3P_1$ (A), $^1S_0 \rightarrow {}^3P_2$ (B) and $^1S_0 \rightarrow {}^1P_1$ (C) transitions[30] are observed in the spectral range of 200–400 nm. A bathochromic shift of the band maxima is observed for [$Sb_2Br_8^{2-}$] compared to the relevant bands in the spectrum of [$Sb_2Cl_8^{2-}$]. This may suggest some increase of the covalent contribution to the Sb–Br bonding. Moreover, the baseline in the spectra of the [$Sb_2Br_8^{2-}$] complex gradually rises compared to the spectrum of [$Sb_2Cl_8^{2-}$]. This is probably caused by a strong ligand-to-metal charge-transfer (LMCT) band, which is strongly delocalized and appears usually as a broad, intense band.[30,32] Due to the lower optical electronegativity[32] as well as the higher oxidation potential of Br^- ions than Cl^-, the energy of the LMCT transition decreases significantly in the case of the

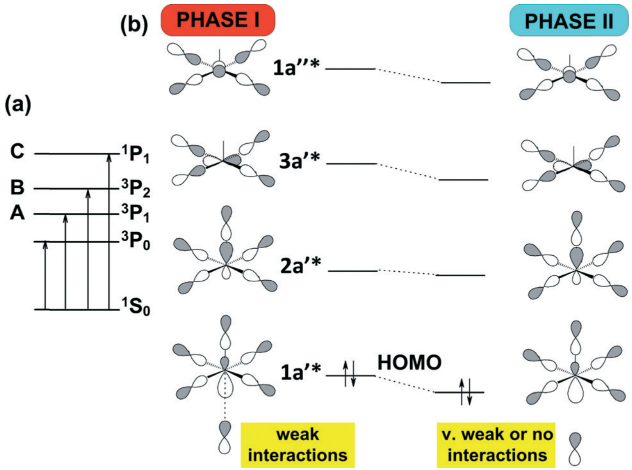

Fig. 6 (a) Representation of the energy-level scheme of the Sb^{3+} ion; (b) qualitative MO scheme of the AL_5 complex (square pyramid with C_s symmetry).

bromide complex. The PT at 222/229 K, related to the structural rearrangement of the [$Sb_2Br_8^{2-}$] anion, is reflected in the UV-vis spectrum. There is a distinct shift of the A band, while the energy of the remaining B and C bands remains essentially unchanged. The qualitative MO scheme for the AL_5 type complex with C_s symmetry (Fig. 6) may be helpful to elucidate such a spectral feature.

Within this simple MO approach, the observed A, B and C bands may be assigned to the $^1A' \rightarrow {}^3A'$, $^1A' \rightarrow {}^3A'$ and $^1A' \rightarrow {}^1A''$ transitions, respectively.

As it was shown in the Single-crystal X-ray diffraction and theoretical structure analysis section, the PT results in certain elongation of two equatorial Sb–Br(2)^i and Sb–Br(3) bond lengths and shortening of the Sb–Br(2) bond on decrease of the temperature. The distance between the sixth Br^- anion and Sb^{3+} cation (Sb–Br(1)^{ii} 3.49 Å) in phase I may suggest a weak interaction between these ions and the formation of a quasi 6-coordinate surrounding of Sb^{3+}. In phase II, the latter interaction is reduced due to significant elongation of the Sb–Br(1)^{ii} distance (3.67 Å). Taking into account these structural changes, one may conclude that the more rigid structure of the anionic complex in phase I becomes less tight in phase II. As a result of the I → II PT, the energy of the antibonding 1a′*, 3a′*, 1a″* orbitals should decrease, while the energy of the 2a′* orbital should be only slightly affected. Within this simple, qualitative model, a certain increase of the energy of the $^1A' \rightarrow {}^3A'$ transition should be expected. Indeed, the energy of the A transition increases by ~900 cm^{-1} on decrease of the temperature, while the energy of A and B bands is practically unchanged.

We have also recorded the luminescence spectra of the compound under study. Interestingly, a red emission was observed at 77 K when the sample was excited with 360 nm light, while it was practically quenched at RT. This raises questions whether the appearance of luminescence at low-temperature is connected with the PT or is it brought about by another reason? Trying to explain this we have measured the luminescence spectra of the [$Sb_2Br_8^{2-}$] complex at different temperatures (Fig. 7).

As it can be seen from Fig. 7, the red emission centered at 650 nm and attributed to the $^1S_0 \rightarrow {}^3P_{1,0}$ transitions appears at 175 K. Below 175 K, the intensity of the $^1S_0 \rightarrow {}^3P_{1,0}$ band gradually increases with decrease of the temperature. At 220 K the luminescence is definitely quenched and therefore cannot provide any information about the PT. The large Stokes shift, 11 120 cm^{-1}, may indicate that the structure of the [$Sb_2Br_8^{2-}$] complex in the excited state is strongly affected compared to that in the ground state.[30,31] This implies a high value of the electron-lattice coupling parameter S and the absence of the vibrational structure. Indeed, the estimated value of the Huang–Rhys[33] coupling constant $S \approx 21$ and the effective phonon energy $\hbar\omega$ = 286 cm^{-1} using eqn (1) and (2) suggest strong vibronic coupling of electronic states with Sb–Br oscillations.

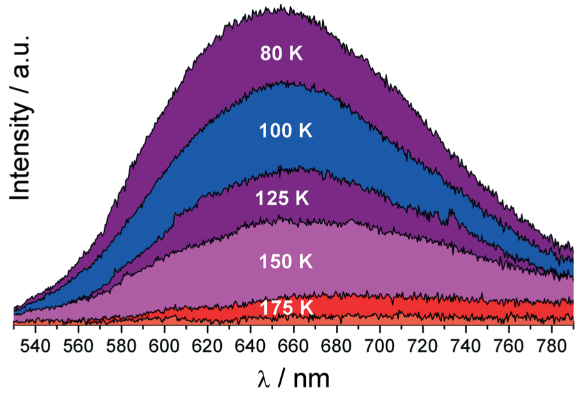

Fig. 7 Emission spectra of the [$Sb_2Br_8^{2-}$] complex at different temperatures, λ_{ex} = 360 nm.

$$\Delta E_S = (2S-1)\cdot\hbar\omega \tag{1}$$

$$\Gamma_T = \hbar\omega\cdot\sqrt{8\ln 2\cdot S\cdot\coth\left(\frac{\hbar\omega}{2kT}\right)} \tag{2}$$

where:

ΔE_S is the Stokes shift/cm^{-1};

Γ_T is the half width of the emission band/cm^{-1};

S is the Huang–Rhys electron-lattice coupling constant;

$\hbar\omega$ is the effective phonon energy/cm^{-1};

k is the Boltzmann constant (0.695 cm^{-1} K^{-1}); and

T is the temperature/K.

As it was shown by Blasse *et al.*, for the case of Bi^{3+} complexes, there is a strong negative correlation (R = −0.97) between the energy difference of the excited $^3P_1$, $^3P_0$ states and the Stokes shift of the emission band.[30b] It may suggest that the energy of the $^3P_1$ state is close to the $^3P_0$ one in our case. These results, namely strong vibronic coupling, close energies of the emission $^3P_1$, $^3P_0$ states as well as a relatively low energy of the LMCT, seem to be reasons for the effective luminescence quenching of the compound under study at room temperature. A more detailed study on the luminescence properties of the compound is outside the scope of this paper.

Dielectric properties

The dielectric response of $[(i\text{-}C_4H_9)_2NH_2]_2Sb_2Br_8$ in the radio-frequency region below RT is illustrated in Fig. 8(a) and (b).

The real part of the dielectric constant, ε', in the vicinity of 222 K falls abruptly, which confirms the first-order character of I → II PT. Over phase I, the imaginary part of the dielectric constant (ε'') shows the characteristic shift of ε''_{max} with frequency towards higher temperatures, which confirms the low-frequency relaxation process. This process may be well described by the Cole–Cole relation:[34]

$$\varepsilon^*(\omega) = \varepsilon_\infty + \frac{\varepsilon_0 - \varepsilon_\infty}{1+(i\omega\tau)^{1-\alpha}} \tag{3}$$

where: ε_0 and ε_∞ are the low and high frequency limits of the dielectric constant, respectively, ω is the angular frequency, τ

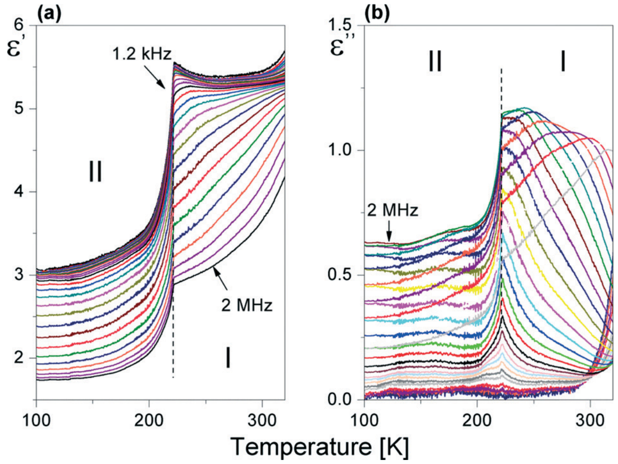

Fig. 8 Temperature dependence of the (a) real (ε′) and (b) imaginary (ε″) parts of the complex dielectric constant (ε*) measured for the powder sample of $[(i\text{-}C_4H_9)_2NH_2]_2Sb_2Br_8$ upon cooling.

is the macroscopic relaxation time and α is a parameter characterizing the distribution of the relaxation times.

The Cole–Cole diagrams at selected temperatures (between 230 and 300 K) are presented in Fig. S4.† The Cole–Cole plots deviate from the semi-circles over the analyzed temperature region, (α ranges between 0.05 and 0.20), which means that we deal with a polydispersive relaxation process approaching 222 K. We have fitted the experimental Cole–Cole plots at selected temperatures with eqn (3) and determined the fitting parameters ε_0, ε_∞ and τ. Since we deal with weak dipole–dipole interactions (the lack of long-range order), we can assume that the macroscopic relaxation time is close to a microscopic one. Thus, the energy barrier E_a can be estimated from the Arrhenius relation:

$$\tau = C\exp\left(\frac{E_a}{kT}\right) \tag{4}$$

The E_a magnitude was estimated to be rather small, *ca.* 8 ± 1.5 kJ mol^{-1} (see Fig. S5†), taking into account the fact that we deal with bulky organic cations.

Proton magnetic resonance studies (^{1}H NMR)

The temperature relations of the proton nuclear relaxation time T_1 for 15 MHz and 25 MHz are shown in Fig. 9(a). There are two different temperature ranges above and below the PT temperature at 229 K. The low-temperature range of the spin–lattice relaxation time function reveals two weakly separated minima characterized by nearly the same depth, which are better separated at the frequency of 15 MHz.

When considering different mechanisms of the proton relaxation occurring in $[(i\text{-}C_4H_9)_2NH_2]_2Sb_2Br_8$, one can distinguish the following possibilities of motions:

(a) Molecular motions of the four methyl groups and otherwise motion of the $[(i\text{-}C_4H_9)_2NH_2{}^+]$ cation (axial motion of the $(i\text{-}C_4H_9)$ side chain attached to the nitrogen atom);

(b) Reorientations of the four methyl groups of two different and structurally inequivalent $[(i\text{-}C_4H_9)_2NH_2{}^+]$ cations; and

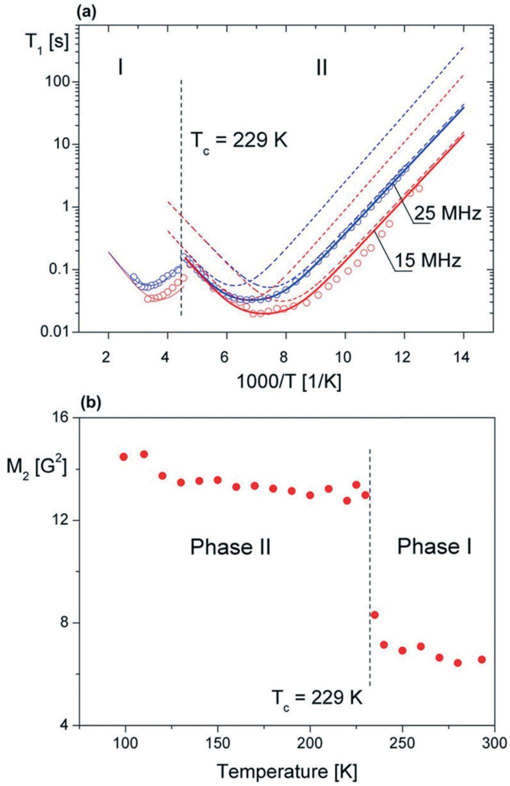

Fig. 9 (a) Temperature dependence of ^{1}H T_1 observed for $[(i\text{-}C_4H_9)_2NH_2]_2Sb_2Br_8$ at 15 MHz and 25 MHz. The solid lines were calculated by using the best-fit parameters given in Table S4.† (b) Temperature dependence of ^{1}H NMR second moment of $[(i\text{-}C_4H_9)_2NH_2]_2Sb_2Br_8$.

(c) The inequivalent two pairs of methyl groups of $(i\text{-}C_4H_9)$ side chains of the same organic cation (see Fig. S6†).

The first possibility, (a), should be rejected because of almost the same values of $T_{1\min}$ and the similar dynamical parameters of both fitted minima which lead to the conclusion that we have the same origin of both component minima. The second possibility, (b), should be also rejected because the X-ray data exclude the presence of structurally inequivalent cations. Therefore, it seems that the third possibility (c) is realized in $[(i\text{-}C_4H_9)_2NH_2]_2Sb_2Br_8$. Both T_1 relaxation time minima originate from a pair methyl groups of the side chain bonded to the N atom in the same cation. Both pairs of CH_3 groups have different molecular dynamics resulting in different temperature dependence trends.

This fact confirms that above 229 K (phase I), the relaxation mechanism of indistinguishable methyl groups dominates. It may also indicate the unification of two previously independent side chain parts of the $[(i\text{-}C_4H_9)_2NH_2{}^+]$ cation *via* spin diffusion. In the T_1 measurements, any other possible reorientation such as the expected axial movement of the side chains is still not visible (more in ESI†).[35–45] The temperature dependence of the second moment M_2 of the ^{1}H NMR line (Fig. 9(b)) has been measured between 99 K and 293 K. With the increase of temperature from 99 K to the PT point at 229 K, the value of ^{1}H M_2 is nearly constant, experiencing only a slight reduction from *ca.* 14.5 G^2 to 13 G^2. At the PT, the M_2 value drops to *ca.* 7 and then continuously decreases down to 6.5 G^2 at 293 K. The calculations of M_2 of the ^1H NMR line for a rigid lattice were made using the van Vleck formula taking into account the homo-nuclear H–H and hetero-nuclear H–N intramolecular interactions.[46] For the H–H interaction, we found $M_{\text{rigid}}^{\text{HH}}$ to be 25.1 G^2 and for the H–N interaction $M_{\text{rigid}}^{\text{HN}}$ was estimated to be *ca.* 3.8 G^2, whereas the inter-cation contribution is about 1 G^2. It should be noticed that even at the lowest temperature (99 K), the expected high value of M_2 is not reached. In turn, the experimental reduced M_2 value of the order of 7 G^2 close to T_c suggests the expected axial motion of $[(i\text{-}C_4H_9)_2NH_2^+]$ cations. The value of M_2 (*ca.* 14 G^2) found below T_c, originates, most probably, from the axial movement of one of both cation side chains (i-butylammonium) or only any partial motion inside side chains of the cation.

Vibrational spectroscopy

In both phases *i.e.* at room temperature (phase I) and at 100 K (phase II), the title crystal is monoclinic and belongs to the $P2_1/c$ (= C_{2h}^5) space group, $Z = 4$. Thus, in the unit cell of the title crystal there are two symmetry equivalent centrosymmetric anions $[Sb_2Br_8^{2-}]$ and four symmetry equivalent diisobutylammonium cations, which occupy the general C_1 sites. The low-temperature phase II is strictly ordered, *i.e.* both anions (octabromodiantimonate(III)) and cations (diisobutylammonium) are ordered. However, in phase I, the diisobutylammonium cations ($(C_4H_9)_2NH_2^{(1+)}$) exhibit disorder, in which both isobutyl groups of each diisobutylammonium cation are distributed between two sites. Simultaneously, the anions remain ordered and preserve the C_i site symmetry.

The numbers of normal modes of the isolated cation of C_1 symmetry (its normal modes can be divided into 3 A-type librational modes, 3 A-type translational modes and 81 A-type internal modes) and those of the isolated anion of C_i symmetry (its 30 normal modes can be divided into: 3 librational modes (3 A_g), 3 translational modes (3 A_u) and 24 (12 A_g + 12 A_u) internal modes) are identical in both phases, respectively. However, for the low-temperature ordered phase II, one may expect an additional splitting of each normal mode due to the Davydov type coupling. Thus, each mode of A-type may split into four ($A_g + B_g + A_u + B_u$) unit cell modes, the A_g-type modes into two ($A_g + B_g$) and the A_u-type modes into two other ($A_u + B_u$) unit cell modes. The results of the fundamental mode analysis for phase II of the title crystal is given in Table S5.† The Davydov type splitting should not appear for the normal modes of cations in the high temperature phase I, due to their disorder therein. A problem then exists – if whether the Davydov type splitting may appear or not for the ordered part (anions) of the crystal in this high temperature phase.

Generally, the positions/wavenumbers of the majority of the bands assigned to the internal vibrations of cations in $[(i\text{-}C_4H_9)_2NH_2]_2Sb_2Br_8$ do not experience any noticeable changes in their positions due to the PT (Fig. S7†). Nevertheless, some bands show a significant continuous and discontinuous change of their positions, intensities and FWHM (full width at half maximum) in the vicinity of T_c (see also Fig. S8–S10†).

Fig. 10(a) shows an evolution of the IR spectra in the range between 1040 and 960 cm^{-1} as a function of temperature. The bands in this wavenumber range arise from the ν_a(CNC), ν_s(CCC) and ν_s(CNC) vibrations. Distinct changes in the position of these bands are observed at *ca.* 230 K (see Fig. 10(b)). For two of these bands, a step-wise change in their position occurs, *i.e.* the band at 963 cm^{-1} (marked as (1)) shifts towards higher wavenumbers, while the one at 974 cm^{-1} (described as (2)) shifts towards lower ones on increasing temperature. The positions of the remaining components are not sensitive to the PT.

The temperature behavior of the bands assigned to the $\delta(NH_2^+)$ vibrations appearing between 1605 and 1530 cm^{-1} (Fig. 11 (a) and (b)) differs clearly from that presented earlier. The higher frequency component (marked as (3)) experiences only a slight anomaly around the T_c, while the lower one

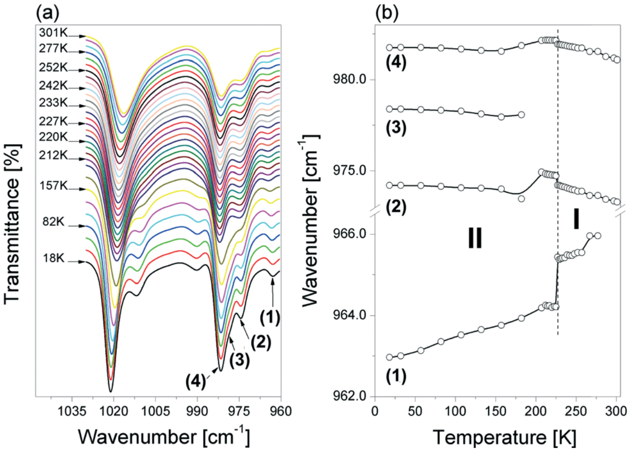

Fig. 10 (a) Temperature evolution of the IR spectra in the $\nu_{s,a}$(CNC) and ν_a(CCC) vibration region (1040–960 cm^{-1}) and (b) the dependence of the wavenumbers of these modes on the temperature change between 18 and 301 K for the $[(i\text{-}C_4H_9)_2NH_2]_2Sb_2Br_8$ crystal. The bands at *ca.* 1012 (sh) and 1021 cm^{-1} (ν_aCNC) are omitted in part (b) of the figure. sh – shoulder.

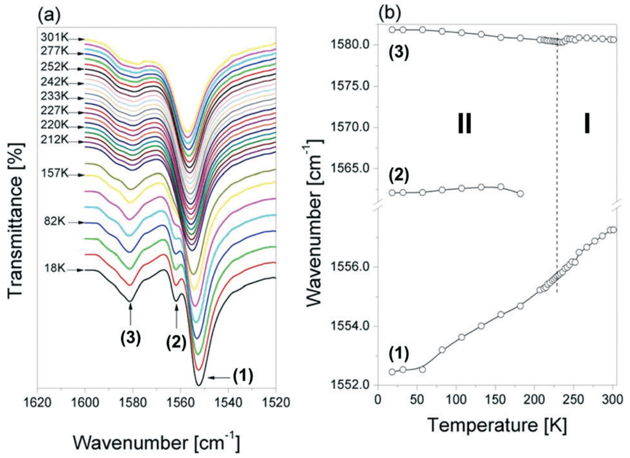

Fig. 11 (a) Temperature evolution of the IR spectra in the $\delta(NH_2^+)$ vibration region (1605–1530 cm^{-1}) and (b) the dependence of the wavenumbers of these modes on the temperature change between 18 and 301 K for the $[(i\text{-}C_4H_9)_2NH_2]_2Sb_2Br_8$ crystal.

(denoted as (1)) shifted towards higher wavenumbers in a continuous way (without visible changes around T_c) on heating. The shoulder (2) at about 1562 cm^{-1} disappears on heating in the low-temperature phase (at about 200 K).

The lowest frequency band observed at 1557 cm^{-1} in this region at room temperature shifts to 1552 cm^{-1} in the spectrum measured at 18 K, however, without any drop of the PT temperature. This can be related to the observed decrease of the N–H⋯O hydrogen bond strength on cooling down, which is clearly indicated by the N⋯Br distances determined for the structure at 250 K (3.355(7), 3.386 Å) and at 100 K (3.540(3) and 3.398(3) Å), respectively (see Table 2). As this band arises from the δNH_2 vibration, therefore its wavenumber may be very sensitive to the strength of the hydrogen bonds in which the protons of this group are involved. With decrease of the strength (*i.e.* increase of the N⋯Br distance), this mode should shift to lower wavenumbers.

Experimental section

Synthesis of the complexes

All reagents used for the syntheses of $[(i\text{-}C_4H_9)_2NH_2]_2Sb_2Br_8$ and $[(i\text{-}C_4H_9)_2NH_2]_2Sb_2Cl_8$ were purchased from commercial sources (Sigma-Aldrich) and used without further purification: diisobutylamine (99%,), Sb_2O_3 (99%), Bi_2O_3 (99.999%), HBr (48%) and HCl (37%).

$[(i\text{-}C_4H_9)_2NH_2]_2Sb_2Br_8$. An aqueous solution of diisobutylamine was added to a stoichiometric amount of Sb_2O_3 in HBr. The obtained precipitate was recrystallized twice from an aqueous solution with an excess of hydrobromic acid. Yellow-transparent single crystals suitable for single-crystal X-ray measurements were grown from a saturated solution by slow evaporation at room temperature. Elemental analysis details: C: 16.62% (theor. 16.81%), N: 2.39% (theor. 2.45%), H: 2.81% (theor. 3.53%).

$[(i\text{-}C_4H_9)_2NH_2]_2Sb_2Cl_8$. Concentrated HCl was added dropwise to a solution containing diisobutylamine in H_2O at 45 °C. After a few days, single crystals of $[(i\text{-}C_4H_9)_2NH_2]_2Sb_2Cl_8$ were grown by slow evaporation from the colorless solution. The crystalline product was twice recrystallized from water. Single transparent, needle-like crystals were characterized by elemental analysis: C: 24.72% (theor. 24.40%), N: 3.23% (theor. 3.56%), H 4.82% (theor. 5.12%).

General

X-ray diffraction studies. The crystallographic measurements were performed on a Kuma KM4CCD four-circle diffractometer. For more details see the ESI.†[47–49] CCDC no. 1475468–1475471.

Thermal properties. Simultaneous thermogravimetric analysis (TGA) and differential thermal analysis (DTA) were performed on a Setaram SETSYS 16/18 instrument in the temperature range of 300–700 K with a ramp rate of 2 K min^{-1}. The scans were performed under flowing nitrogen (flow rate: 1 dm^3 h^{-1}). DSC heating curves were obtained using a Perkin Elmer 8500 differential scanning calorimeter calibrated using *n*-heptane and indium. Hermetically sealed Al pans with the polycrystalline material were prepared in a controlled-atmosphere N_2 glove box. The measurements were performed between 100 and 290 K. The thermal hysteresis was estimated from the scans performed at various rates (20, 10 and 5 K min^{-1}) extrapolated to the scanning rate of 0 K min^{-1}.

Dilatometric measurements. Dilatometric measurements were performed using a Perkin Elmer TMA-7 thermomechanical analyzer in the temperature range of 150–280 K with the scanning rate of 3 K min^{-1}.

Dielectric spectroscopy. The complex dielectric permittivity, $\varepsilon^* = \varepsilon' - i\varepsilon''$, was measured by a E4980A Precision LCR Meter within the frequency range of 500 Hz–2 MHz and in the temperature range within 100–300 K. The dimensions of the sample were of the order 3 × 2 × 1 mm^3. The overall error for the real and imaginary parts of the complex dielectric permittivity was less than 5% and 10%, respectively. Silver electrodes were printed on opposite faces.

Optical measurements. The optical microscopy observation was carried out by using an Olympus BX53 combined with a LINKAM THM-600 heating/cooling stage, where the temperature was stabilized to within 0.1 K.

UV-vis absorption spectra. The UV-vis absorption spectra of the compound under study were recorded using a Cary 5000 UV/vis/NIR. The spectra of the powder were measured at different temperatures (200–293 K) in a continuous flow helium cryostat (Optistat, Oxford).

Luminescence spectra. Luminescence spectra of crystals under study were measured on an Edinburgh Instruments FLS 920 spectrometer in the temperature range of 77–298 K. The temperature measurements of crystals were performed in a nitrogen cryostat Optistat DN (Oxford Instruments).

Proton magnetic resonance (^1H NMR). The NMR T_1 relaxation times of the hydrogen nuclei NMR measurements were determined on an ELLAB TEL-Atomic PS 15 spectrometer working at the frequencies of 15 and 25 MHz in the temperature range from 80 K to 300 K. The T_1 relaxation times were determined by the saturation method. The second moment of ^1H NMR line was measured in the temperature range from 99 K to 293 K by a continuous wave ELLAB TEL-Atomic CWS 12-50 spectrometer working on protons at the frequency of 28.2 MHz. The M_2 values were found by numerical integration of the absorption curve derivatives. The temperature of the sample was controlled by a UNIPAN 660 temperature controller operating on a Pt 100 sensor providing long time temperature stability better than 1 K. All measurements were made on heating the sample from the liquid nitrogen temperature. The errors in the measurements of T_1 were estimated to be about 5%. The measured sample was degassed at room temperature and sealed under vacuum in a glass ampoule.

IR measurements. The infrared spectra of $[(i\text{-}C_4H_9)_2NH_2]_2Sb_2Br_8$ were recorded in a wide temperature range (from 18 to 301 K) in KBr pellets with a Bruker IFS-88 spectrometer in the wavenumber range of 4000–500 cm^{-1} with a resolution of 1 cm^{-1}. An APD Cryogenics Displex

Closed Cycle Refrigeration System, Model CSW-202 was used for the temperature dependence studies. The temperature of the sample was maintained with an accuracy of 0.1 K by a Scientific Instruments INC controller Series 5500. The Grams/368 Galactic Industries program was used for numerical fitting of the experimental data. The Gaussian functions were used for fitting the infrared bands. Powder FT-Raman spectra were recorded using an FRA-106 attached to a Bruker IFS-88 using a Nd:YAG diode pump laser. The measurements were performed over the wavenumber range of 3500–80 cm^{-1} at room temperature with a resolution better than 2 cm^{-1}. The bands characteristic of the internal vibrations of the diisobutylamine appear in the measured IR spectra (see Fig. S6†). The wavenumbers of the bands observed in these spectra are listed in Table S7,† together with assignments proposed on the basis of normal coordinate analysis available in the literature for the isopropylamine,[50–52] isobutylammonium cations in $[i\text{-}(C_4H_9)_2NH_2]_3Bi_2Br_9$ (ref. 53) and isopropylammonium cations in $[i\text{-}(CH_3)_2CHNH_3]_4Cd_3Cl_{10}$.[54,55]

Computational details. To localise the key stationary points on the potential energy surface (PES) of the $[(i\text{-}C_4H_9)_2NH_2]_2Sb_2Br_8$ crystal, a series of full geometry and cell parameter optimizations with the London-type empirical correction for dispersion interactions, as proposed by Grimme,[56] together with the vibrational frequency calculations in harmonic approximation were undertaken. The calculations were performed using the CRYSTAL09 (ref. 57) program, utilizing the DFT method with the B3LYP[58–61] hybrid density functional with the two shrinking factors (5,5) to generate a commensurate grid of *k*-points in reciprocal space, following the Monkhorst–Pack method.[62] Calculations were carried out with the consistent Gaussian basis sets of triple-zeta valence with polarization quality for solid-state calculations (pob_TZVP_2012), as proposed by Peintinger, Vilela Oliveira, and Bredow.[63] In addition, calculations were carried out with the atomic Effective Core Potential (ECP) for the antimony atom (Sb_DURAND-21d1G_causa_1991), implemented by Barthelat and Durand[64] and tested successfully for solid-state calculations by Causà[65] and co-workers. The calculation of vibrational frequencies in CRYSTAL09 was performed at the *Γ*-point.[57,66]

Conclusion

In this paper we have reported the physicochemical properties of the $[(i\text{-}C_4H_9)_2NH_2]_2Sb_2Br_8$ crystal, which was found to undergo isomorphous PT of the first-order type at 222/229 K (cooling–heating). The molecular mechanism of this transition is rather complex because two contributions should be considered. The calorimetric studies allow us to estimate the transition entropy value (ΔS_{tr} = 26 J mol^{-1} K^{-1}) which clearly indicates an "order–disorder" contribution to the PT. The structure of $[(i\text{-}C_4H_9)_2NH_2]_2Sb_2Br_8$ consists of $[Sb_2Br_8^{2-}]$ anions with a geometry of two square pyramids sharing a basal edge and diisobutylammonium cations which are highly disordered in phase I and fully ordered in phase II. The PT in the cooling mode is additionally related to the smoothing of the Br–Sb–Br angle distortion of the $[SbBr_4^-]$ units. In turn, deepening of distortion in the bridging part of the $[Sb_2Br_8^{2-}]$ unit and shifting as well as rotation of the $[Sb_2Br_8^{2-}]$ units in relation to each other, leading to the enormous crystal lattice distortion compared with phase I, cause a better fit of diisobutylammonium cations to the anionic moiety. These changes within the anionic moieties are treated as a "displacive" contribution to the mechanism of PT.

The dielectric dispersion measurements confirmed the dynamical disorder of the cationic dipolar units in phase I which is reflected in the presence of the low frequency relaxation process. It should be added that librational motions of the whole $[Sb_2Br_8^{2-}]$ anions with respect to their symmetry centre in phase I may also contribute to the dielectric relaxation. The contribution of the cation motion to the molecular mechanism of PT is evidently reflected in the drastic reduction of the second moment value of the ^1H NMR line at 229 K. These studies lead to the following conclusions:

(a) In the temperature range of 50–229 K (phase II), only the C_3-type motion of CH_3 groups contributes to the relaxation time T_1. Dynamical inequality of both side chains of the $[(i\text{-}C_4H_9)_2NH_2^+]$ cation in this phase is postulated.

(b) The methyl group relaxation still prevails over phase I (above 229 K). On the other hand, two different axial reorientations on the opposite side of the chain of the $[(i\text{-}C_4H_9)_2NH_2^+]$ cation have been observed in the second moment studies.

The anomalies found in the temperature dependent infrared spectra around T_c are generally quite subtle. Most of the modes exhibit different temperature coefficients describing the temperature dependence of their wavenumbers. The discontinuous changes of the band positions are observed for some modes around 229 K, but they are very small. This may be explained by the fact that the space group of the neighboring phases and the environment of the cations in the crystal lattice do not change throughout the PT.

Infrared and Raman spectra have also been recorded for the studied $[(i\text{-}C_4H_9)_2NH_2]_2Sb_2Br_8$ crystal and comparative vibrational analysis has been performed. Vibrational analysis is very important since it proves that the results of the static structure optimisation are correct. The comparison between experimental and calculated vibrational frequencies for the studied crystal has been presented in Table S6.† Due to the fact that the calculation of vibrational frequencies was performed at the gamma-point and also in the harmonic approximation, the calculated wavenumbers presented in Table S6† are shifted towards higher wavenumbers by about 200 cm^{-1} or less. The shift values of the frequency of vibration caused by harmonic approximation seem to decrease with decrease of the wavenumbers of oscillations. The stretching vibrations of the Sb–Br bonds appear in the range from 220 to 100 cm^{-1} and their bands are relatively intense. This is a typical position of the stretching bands for molecular [Sb–Br] systems and may be an important contribution to the stability of the crystal structure. The occurrence of these stretching bands in the region of low frequencies indicates that the [Sb–Br] crystal is held by very weak interactions. Consequently, we have observed appearance of easy reorganisations of the chemical bonds in the molecular complex, which favours the phase transition possibility.

Acknowledgements

This work was supported by the National Science Centre; grant no. 2013/11/D/ST8/03297 (A. Piecha-Bisiorek). One of the authors (Piotr Durlak, Ph.D.) would like to gratefully acknowledge the Wroclaw Centre for Networking and Supercomputing (WCSS) for allocation of computer time on the BEM Cluster.

References

1 J. F. Scott, *Ferroelectric Memories*, Springer, Berlin, 2000.
2 R. Waser, *Nanoelectronics and information technology*, Wiley-VCH, Weinheim, Germany, 2003.
3 Z. G. Ye, *Handbook of advanced dielectric, piezoelectric and ferroelectric materials: Synthesis, properties and applications*, Woodhead Publishing, Cambridge, UK, 2008.
4 J. F. Scott, *Science*, 2007, **315**, 954.
5 M. Owczarek, P. Szklarz, R. Jakubas and A. Miniewicz, *Dalton Trans.*, 2012, **41**, 7285.
6 X. H. Zhao, X. C. Huang, S. L. Zhang, D. Shao, H. Y. Wei and X. Y. Wang, *J. Am. Chem. Soc.*, 2013, **135**, 16006.
7 J. Burschka, N. Pellet, S.-J. Moon, R. Humphry-Baker, P. Gao, M. K. Nazeeruddin and M. Grätzel, *Nature*, 2013, **499**, 316.
8 M. M. Lee, J. Teuscher, T. Miyasaka, T. N. Murakami and H. J. Snaith, *Science*, 2012, **338**, 643.
9 W. Zhang, H. Y. Ye, R. Graf, H. W. Spiess, Y. F. Yao, R. Q. Zhu and R.-G. Xiong, *J. Am. Chem. Soc.*, 2013, **135**, 5230.
10 S. H. Park, I. H. Oh, S. Park, Y. Park, J. H. Kim and Y. D. Huh, *Dalton Trans.*, 2012, **41**, 1237.
11 H. Xu, R. Chen, Q. Sun, W. Lai, Q. Su, W. Huang and X. Liu, *Chem. Soc. Rev.*, 2014, **43**, 3259.
12 Y. Zhang, H.-Y. Ye, H. L. Cai, D. W. Fu, Q. Ye, W. Zhang, Q. H. Zhou, J. L. Wang, G. L. Yuan and R.-G. Xiong, *Adv. Mater.*, 2014, **26**, 4515.
13 L. Sobczyk, R. Jakubas and J. Zaleski, *Pol. J. Chem.*, 1997, **71**, 265 (and references cited therein).
14 J. Jóźków, R. Jakubas, G. Bator and A. Pietraszko, *J. Chem. Phys.*, 2001, **114**, 7239.
15 R. Jakubas, A. Piecha, A. Pietraszko and G. Bator, *Phys. Rev. B*, 2005, **72**, 104107.
16 A. Piecha, A. Pietraszko, G. Bator and R. Jakubas, *J. Solid State Chem.*, 2008, **118**, 1155.
17 A. Piecha, A. Białońska and R. Jakubas, *J. Phys.: Condens. Matter*, 2008, **20**, 325224.
18 R. Jakubas, U. Krzewska, G. Bator and L. Sobczyk, *Ferroelectrics*, 1988, 77, 129.
19 R. Jakubas, *Solid State Commun.*, 1989, **69**, 267.
20 R. Jakubas, Z. Czapla, Z. Galewski and L. Sobczyk, *Ferroelectr., Lett. Sect.*, 1986, **5**, 143.
21 J. Zaleski and A. Pietraszko, *Acta Crystallogr., Sect. B: Struct. Sci.*, 1996, **52**, 287.
22 W. Bi, N. Leblanc, N. Mercier, P. Auban-Senzier and C. Pasquier, *Chem. Mater.*, 2009, **21**, 4099.
23 A. Piecha, A. Białońska and R. Jakubas, *J. Mater. Chem.*, 2012, **22**, 333.
24 G. Xu, Y. Li, W.-W. Zhou, G.-J. Wang, X.-F. Long, L.-Z. Cai, M.-S. Wang, G.-C. Guo, J.-S. Huang, G. Bator and R. Jakubas, *J. Mater. Chem.*, 2009, **19**, 2179.
25 R. Jakubas, Z. Ciunik and G. Bator, *Phys. Rev. B*, 2003, **67**, 024103.
26 D.-W. Fu, W. Zhang, H.-L. Cai, J.-Z. Ge, Y. Zhang and R.-G. Xiong, *Adv. Mater.*, 2011, **23**, 5658.
27 A. Piecha, A. Gągor, R. Jakubas and P. Szklarz, *CrystEngComm*, 2013, **15**, 940.
28 D.-W. Fu, H.-L. Cai, Y. Liu, Q. Ye, W. Zhang, Y. Zhang and X.-Y. Chen, *Science*, 2013, **25**, 425.
29 A. Piecha-Bisiorek, A. Białońska, R. Jakubas, P. Zieliński, M. Wojciechowska and M. Gałązka, *Adv. Mater.*, 2015, **27**, 5023.
30 (*a*) A. Vogler, A. Paukner and H. Kunkely, *Coord. Chem. Rev.*, 1990, **97**, 285; (*b*) G. Blasse, *Electronic and Vibronic Spectra of Transition Metal Complexes I in Topics in Current Chemistry*, ed. H. Yersin, 1994, vol. 171, p. 1.
31 (*a*) A. Vogler and H. Nikol, *Comments Inorg. Chem.*, 1993, **4**, 245; (*b*) T. A. Albright, J. K. Burdett and M.-H. Whangbo, *Orbital Interactions in Chemistry*, Willey, 2013.
32 C. K. Jørgensen, *Absorption Spectra and Chemical Bonding in Complexes*, Oxford, 1964.
33 K. Huang and A. Rhys, *Proc. R. Soc. London, Ser. A*, 1950, **204**, 406.
34 K. S. Cole and R. H. Cole, *J. Chem. Phys.*, 1941, **9**, 341.
35 D. E. Woessner, *J. Chem. Phys.*, 1962, **36**, 1.
36 W. Medycki, Z. Zimpel, N. Piślewski and R. Jakubas, *Solid State Commun.*, 1990, **76**, 869.
37 W. Medycki, N. Piślewski and R. Jakubas, *Solid State Nucl. Magn. Reson.*, 1993, **2**, 197.
38 W. Medycki, R. Jakubas, N. Piślewski and J. Lefebvre, *Z. Naturforsch., A: Phys. Sci.*, 1993, **48**, 748.
39 J. Zaleski, W. Medycki, N. Piślewski and R. Jakubas, *Phys. Status Solidi A*, 1994, **144**, 81.
40 J. Zaleski, W. Medycki, N. Piślewski and R. Jakubas, *Phys. Status Solidi B*, 1995, **190**, 199.
41 W. Medycki, *Solid State Nucl. Magn. Reson.*, 1999, **13**(4), 213.
42 W. Medycki, *Solid State Nucl. Magn. Reson.*, 1999, **14**, 137.
43 W. Medycki and R. Jakubas, *Solid State Nucl. Magn. Reson.*, 1999, **15**(2), 73.
44 M. Wojtaś, R. Jakubas, Z. Ciunik and W. Medycki, *J. Solid State Chem.*, 2004, **177**, 1575.
45 B. Kulicka, R. Jakubas, Z. Ciunik, G. Bator, W. Medycki, J. Świergiel and J. Baran, *J. Phys. Chem. Solids*, 2004, **65**, 871.
46 V. Vleck, *Phys. Rev.*, 1948, **74**, 1168.
47 *CrysAlis RED, ver. 1.171*, Oxford Diffraction Poland, 1995–2003.
48 R. C. Clark and J. S. Reid, *Acta Crystallogr., Sect. A: Found. Crystallogr.*, 1995, **51**, 887.
49 G. M. Sheldrick, *Acta Crystallogr., Sect. A: Found. Crystallogr.*, 2008, **64**, 112.

50 D. Zeroka, J. O. Jensen and A. C. Samuels, *Int. J. Quantum Chem.*, 1999, 72, 109.

51 J. R. Durig, J. J. Klaassen, I. D. Darkhalil, W. A. Herrebout, J. J. Dom and B. J. van der Veken, *J. Mol. Struct.*, 2012, **1009**, 30.

52 Y. Hamada, M. Tsuboi, M. Nakata and M. Tasumi, *Chem. Phys.*, 1988, **125**, 55.

53 J. Jóźków, G. Bator, R. Jakubas and J. Baran, *J. Mol. Struct.*, 1998, **450**, 247.

54 B. Staśkiewicz, J. Baran and Z. Czapla, *J. Phys. Chem. Solids*, 2013, **74**, 1848.

55 N. Alpert, W. Keiser and H. Szymanski, *IR: Theory and Practice of Infrared Spectroscopy*, Plenum Press, New York, 1964 and 1970.

56 S. J. Grimme, *J. Comput. Chem.*, 2006, **27**, 1787.

57 R. Dovesi, V. R. Saunders, C. Roetti, R. Orlando, C. M. Zicovich-Wilson, F. Pascale, B. Civalleri, K. Doll, N. M. Harrison, I. J. Bush, Ph. D'Arco and M. Llunell, *CRYSTAL09 User's Manual*, University of Torino, Torino, 2009.

58 A. D. Becke, *J. Chem. Phys.*, 1993, **98**, 5648.

59 P. J. Stephens, F. J. Devlin, C. F. Chabalowski and M. J. Frisch, *J. Phys. Chem.*, 1994, **98**, 11623.

60 K. Kim and K. D. Jordan, *J. Phys. Chem.*, 1994, **98**, 10089.

61 C. Lee, W. Yang and R. G. Parr, *Phys. Rev. B: Condens. Matter Mater. Phys.*, 1988, **37**, 785.

62 H. J. Monkhorst and J. D. Pack, *Phys. Rev. B: Solid State*, 1976, **13**, 5188.

63 M. F. Peintinger, D. Vilela Oliveira and T. Bredow, *J. Comput. Chem.*, 2013, **34**, 451.

64 P. Durand and J. C. Barthelat, *Theor. Chim. Acta*, 1975, **38**, 283.

65 M. Causà, R. Dovesi and C. Roetti, *Phys. Rev. B: Solid State*, 1991, **43**, 11937.

66 R. Dovesi, R. Orlando, B. Civalleri, C. Roetti, V. R. Saunders and C. M. Zicovich-Wilson, *Z. Kristallogr.*, 2005, **220**, 571.